Flexible fibers in turbulence

Cristian Marchioli,[1] Marco Edoardo Rosti,[2] and Gautier Verhille[3]

[1]Department of Engineering and Architecture, University of Udine, Udine, Italy, 33100; marchioli@uniud.it
[2]Complex Fluids and Flows Unit, Okinawa Institute of Science and Technology Graduate University, 1919-1 Tancha, Onna-son, Okinawa Japan, 904-0495; marco.rosti@oist.jp
[3]Aix Marseille Univ, CNRS, Centrale Med, IRPHE, F-13013 Marseille, France; gautier.verhille@cnrs.fr

Xxxx. Xxx. Xxx. Xxx. YYYY. AA:1–27

https://doi.org/10.1146/((please add article doi))

Copyright © YYYY by the author(s). All rights reserved

Keywords

turbulence, fibers, flexibility

Abstract

In this article, we review recent progress in the fundamental understanding of the motion of flexible fibers in turbulent flow, made through multiscale experiments and simulations. Emphasis is given to problems involving flexible fibers that can be conveniently described with discrete and continuum models closely related to the slender body theory. Current state-of-the-art measurement and simulation methods, including optical techniques, Euler-Lagrange approaches for tracking large swarms of fibers, and recent methodologies for simulating finite-size fibers are discussed. The capabilities of simulations and experiments are surveyed in connection with the current physical understanding of how flexible fibers interact with the full spectrum of length and time scales of turbulence. We review the phenomenological and statistical features of fiber dispersion and spatial distribution. We also discuss the relevant aspects of fiber rotation and deformation, highlighting their connection with mechanisms such as fragmentation and turbulence modulation, which are known to exhibit peculiar features in the case of flexible fibers. We conclude our analysis by providing an outlook on future research direction paths, open methodological issues and expected advances, in particular associated to the study of flexible particles in a broader sense.

1. INTRODUCTION

Flexible fibers are common in many industrial and natural turbulent flows, where they are characterized by a wide range of sizes (length, aspect ratio), specific density, and flexibility, a property that is typically associated to the Young modulus of the material composing the fiber. Well-known examples are fibers in the pulp and paper industry (Lundell et al. 2011, Switzer & Klingenberg 2004) or microplastics and algae in oceanic environments (Sugathapala et al. 2025, Bergfreund et al. 2024, Parrella et al. 2024, du Roure et al. 2019). More recently, studies of the long-range transport of microplastic fibers in the atmosphere (Bhowmick et al. 2024, Candelier et al. 2024, Tatsii et al. 2023) have appeared in the literature. An innovative application of flexible fibers is related to the use of buckled flexible filaments as vortex generators to enhance heat transfer in heat sink systems and limit the energy consumption of electronic devices (Chen et al. 2024). Flexible fibers are also found is gas–solid fluidization systems loaded with fibrous granular materials (Xu et al. 2008).

Driven by the practical relevance of all these applications, the problem of turbulent flows laden with flexible fibers has attracted growing attention within the multiphase flow community over the last decade. Significant progress in our understanding of these flows has been made, thanks to unprecedented advances in available measurement and simulation techniques (Giurgiu et al. 2024, Olivieri et al. 2022b). This review is indeed motivated by the need to summarize the most recent findings that concern the translation, rotation and deformation of flexible fibers dispersed in a turbulent flow, highlighting the main phenomenological and statistical features but also surveying the experimental and numerical investigation techniques that are currently adopted. Because the focus is on turbulent flows, this review provides a natural complement to that by du Roure et al. (2019), where the behavior of flexible fibers in viscous flows at low Reynolds numbers was discussed.

The capability of the fibers to deform under the action of a turbulent flow, associated to the non-spherical shape of the fibers, increases significantly the number of degrees of freedom and may add much complexity to the interaction that the fibers have with the different scales of motion (which are defined in the sidebar Turbulent Scales). This leads to significant departures from the ideal case of spherical particles, but also from the case of rigid fibers, which has been nicely addressed in the review by Voth & Soldati (2017). The resulting dynamical behavior, governed by translation, rotation and deformation, is difficult to reproduce through models and simulations, also due to the complexity of the Navier–Stokes equations as opposed to the relative simplicity of the Stokes equations that can be used at low Reynolds numbers. It is equally challenging to make measurements with suitable space and time resolution, in view of the strong fiber anisotropy. These tasks are particularly demanding for fibers that have a high aspect ratio, which most often exhibit the strongest tendency to deform. In this review, we focus our analysis precisely on this kind of fibers, because of their practical importance: High-aspect-ratio fibers are very common in many industrial and environmental processes, as well as in fundamental research, where they are usually employed to run reliable experiments. Considering that fibers occur in a dazzling variety of shapes, we further concentrate our discussion to fibers with circular cross section, constant diameter, and straight at equilibrium.

Although we consider a rather specific type of particles, the body of research is still vast. Therefore, we limit our attention to the case of archetypal turbulent flows (homogeneous turbulence and wall-bounded flows) laden with flexible fibers that are heavier than or at most with the same density as the incompressible Newtonian fluid. This choice is in line with recent reviews that have discussed the behavior of spherical (Brandt & Coletti 2022)

TURBULENT SCALES

The inertial range of turbulence is the region of the turbulent kinetic energy spectrum in which turbulent kinetic energy is purely transferred to smaller scales, where it is eventually dissipated. This region is comprised between the integral length L_I, at which the energy is injected into the flow, and the Kolmogorov length $\eta_K = (\nu^3/\epsilon)^{1/4}$, at which energy dissipation occurs. Here, $\nu = \mu/\rho$ is the fluid kinematic viscosity and ϵ is the energy dissipation rate per unit mass. The small scale dynamics of the flow is characterized by the Kolmogorov time $\tau_K = (\nu/\epsilon)^{1/2}$, and the typical life time of a vortical structure with size ℓ within the inertial range is $\tau_\ell = \tau_K(\ell/\eta_K)^{-2/3}$.

and non-spherical (Voth & Soldati 2017) particles in turbulence. We begin by presenting the parameter space, as defined by convenient nondimensional numbers, and the dynamical regimes identified therein. We then continue by discussing the behavior of individual fibers: A proper understanding of this behavior is essential to set the stage for future studies of the transport, dispersion and settling in turbulent suspensions, for which, however, additional physical effects such as intra-fiber and inter-fiber interactions must be considered.

2. Parameter space and non-dimensional numbers

To understand the relevant parameter space and non-dimensional numbers that can be used to characterize a turbulent suspension of flexible fibers, let us start by considering the simplest theoretical framework that can be invoked to characterize their deformations. We assume here that the fibers are made of a Hookean material, so they are purely elastic (meaning they exhibit no viscoelasticity) and obey linear elasticity. These deformations can be described by the Euler-Bernoulli beam theory, in which the conformation of the fiber is characterized by its neutral axis, defined as the axis along which the longitudinal stresses and strains of the deformed fiber are equal to zero in the absence of stretching or compression. For a homogeneous cylindrical fiber, this axis corresponds to the geometric centroid of the cross section. In most of the cases, the equation used to describe the evolution of the neutral axis is the Euler-Bernoulli equation, the derivation of which can be found in classical textbooks (Landau & Lifshitz 1959, Audoly & Pomeau 2010):

$$\sigma\partial_t^2\mathbf{X} - \partial_s(T\partial_s\mathbf{X}) + B\partial_s^4\mathbf{X} = \mathbf{F}\,. \qquad 1.$$

Here, s is the curvilinear coordinate, $\mathbf{X}$ denotes the position of a point on the neutral axis and σ and B are the linear density and bending modulus of the fiber, respectively. For a cylindrical fiber of length l, diameter d, density ρ_f and Young modulus E, one gets $\sigma = \pi d^2\rho_f/4$ and $B = \pi E d^4/64$. In addition, $T = \int f_\parallel \mathrm{d}s + B|\partial_{ss}\mathbf{X}|^2$ is the tension and $f_\parallel$ the parallel component of the linear force applied to the fiber. On the left-hand side of Equation 1, the first term accounts for fiber inertia, the second term corresponds to the contribution of the tangential stress and is related to fiber extensibility, and the third term represents the resistance to bending. The term on the right-hand side corresponds to the perpendicular component of the external forces, including the hydrodynamic ones. In the slender body approximation, the external forces reduce to to $\bar{\eta}(\mathbf{u} - \partial_t\mathbf{X})$, with $\bar{\eta}$ the viscosity tensor and $\mathbf{u} - \partial_t\mathbf{X}$ the slip velocity between the fluid and the fiber. It has

STOKES NUMBER AND REYNOLDS NUMBER FOR A FIBER

The Stokes number is generally defined as $St = \tau_f/\tau$, where $\tau_f = \rho_f d^2/18\mu$ is the translational relaxation time of the fiber, with ρ_f the fiber density and d the fiber cross-sectional diameter, and τ is the characteristic timescale of the flow. The definition of τ depends on the properties of the flow. In Homogeneous Isotropic Turbulence (HIT), a standard approach is to set $\tau = \tau_K$ for short fibers (with length $l \simeq \eta_K$) and $\tau = \tau_K(L_I/\eta_K)^{2/3}$ for long fibers (with $l \simeq L_I >> \tau_K$). This last relation yields:

$$St = \frac{\rho_f}{\rho}\left(\frac{d}{\eta_K}\right)^{4/3}\left(\frac{d}{l}\right)^{2/3}. \qquad 2.$$

In wall-bounded turbulence, it is customary to set $\tau = \nu/u_*^2$ with u_* the friction (or shear) velocity.

The fiber Reynolds number is generally defined as $Re_f = |\mathbf{u} - \mathbf{v}|\mathcal{L}/\nu$, where $\mathbf{u} - \mathbf{v}$ is the fiber slip velocity relative to the fluid, and $\mathcal{L}$ is a characteristic dimension of the fiber, e.g. l or d. The calculation of the slip velocity may change depending on the specific fiber model adopted. For example, when the fiber is modeled as a chain of elements (see Sec. 3.2.1), the slip velocity is calculated for each element in the chain, using the velocities at the center of mass of the element and considering its orientation, as done in Dotto & Marchioli (2019). When the fiber is modeled as a homogeneous inextensible elastic filament (see Sec. 3.2.2), the difference $\mathbf{\Delta u}$ between the fiber velocity at its midpoint and the local fluid velocity, averaged within a spherical shell centered on the midpoint, is used, as done in Rosti et al. (2018a). This yields $Re_p = d\sqrt{\langle \mathbf{\Delta u} \cdot \mathbf{\Delta u} \rangle}/\nu$. The angular brackets $\langle\rangle$ denote an average over all fibers in the flow.

to be noticed that Equation 1 neglects the torsion of the fiber, an assumption that will be justified thereafter. Equation 1 is complemented with an appropriate set of boundary conditions: $\partial^3\mathbf{X}/\partial s^3|_{s=l} = \mathbf{0}$ and $\partial^2\mathbf{X}/\partial s^2|_{s=l} = \mathbf{0}$ at the free ends of the fiber, along with $T|_{s=l} = 0$. The Euler-Bernoulli equation, in the absence of any external forcing, is passable of a normal mode analysis yielding the natural frequency $f_{\rm nat} \approx 22.3733/(dl^2)\sqrt{\gamma/(\sigma\pi^3)}$, which plays a significant role in determining the dynamical response of the filaments.

For fibers, three types of deformation can be defined: bending, stretching and twisting. The timescales that characterize these deformations depend on the importance of the viscous term in Equation 1. If the viscous term is larger than the inertial one, the regime is called over-damped, whereas a so-called under-damped regime is established when the viscous term is negligible. These two regimes can by parameterized by the Stokes number (see sidebar Stokes Number and Reynolds Number for a Fiber). In the over-damped regime (resp. under-damped), $St \ll 1$ (resp. $St \gg 1$), and the typical timescale is the relaxation time (resp. the period of oscillation T_o), given by the ratio of the bending term and the viscous (resp. inertial) term in the Euler-Bernoulli equation. In this section, we will first focus on the over-damped regime ($St \ll 1$) for which fiber deformations have been characterised extensively.

The characteristic timescale of deformation can be estimated by balancing the elastic term and the viscous damping term in the limit of fluid at rest and linear dissipation (Powers 2010). Note that, in reality, the viscous drag tensor is not strictly isotropic but only its order of magnitude is needed here to estimate the timescale. For bending, the elastic term $B\partial_s^4\mathbf{X}$ scales as $B\delta/l^4$, with δ the amplitude of the deformation, and the viscous term $\mu\partial_t\mathbf{X}$

RIGID VS FLEXIBLE

The flexibility of a fiber can be quantified using the characteristic length $\ell_e = B^{1/4}/(\rho\mu\epsilon)^{1/8}$, which depends on the bending modulus B of the fiber, on the fluid properties (μ, ρ) and on the flow properties, parameterized by ϵ. Fibers with length $l \gtrsim \ell_e$ are classified as flexible, fibers with $l \ll \ell_e$ are classified as rigid. In the following, we refer to ℓ_e as linear elastic length, since it corresponds to a deformation regime where the non-linear term in the Euler-Bernoulli equation is negligible.

scales as $\mu\delta/\tau_b$. Thus, the relaxation timescale of bending, τ_b, is given by:

$$\tau_b \sim \frac{\mu l^4}{B} \sim \frac{\mu l^4}{E d^4}\,, \tag{3.}$$

for a homogeneous cylindrical fiber. The same force balance can be done to estimate the stretching timescale, τ_s. For this kind of deformation, the elastic term scales as $Ed^2\delta/l$ and the viscous one as $\mu l\delta/\tau_s$, thus leading to:

$$\tau_s \sim \frac{\mu l^2}{E d^2}\,. \tag{4.}$$

The characteristic timescale of twisting, τ_t, is given by a torque balance rather than a force balance. In this case, the linear viscous torque is $d\mu\partial_t(d\theta)$, and the elastic torque is $C_t\partial_{ss}\theta \sim EC_t\theta/l^2$, where C_t is the torsional rigidity, which scales as $C_t \sim d^4$ for a cylindrical fiber. The twisting timescale is thus given by:

$$\tau_t \sim \frac{d^2 l^2 \mu}{E C_t} \sim \frac{\mu l^2}{E d^2}\,. \tag{5.}$$

Comparing these three timescales, it can be noticed that the relaxation time of bending is much longer than the relaxation time of both stretching and twisting when the fiber aspect ratio is large ($l \gg d$), since both τ_b/τ_s and τ_b/τ_t scale as $(l/d)^2 \gg 1$. For this reason, most studies have focused only on bending, neglecting stretching and twisting, with the fiber inextensibility enforced by the tension term T in the Euler-Bernoulli equation. In this review, only the bending of inextensible fibers will be discussed. This discussion can be extended to the under-damped regime by replacing the relaxation time with the period of oscillation T_o, obtained by balancing the inertial term $\sigma\partial_t^2\mathbf{X}$, which scales as $\sigma\delta/T_o^2$, and the bending elastic term $B\partial_s^4\mathbf{X}$, which still scales as $B\delta/l^4$. This balance yields:

$$T_o \sim \left(\frac{\sigma l^4}{B}\right)^2 \sim \left(\frac{\sigma l^4}{E d^4}\right)^2. \tag{6.}$$

Throughout the remainder of this review, the deformations of a fiber will be characterized by its deformability, measured by the ratio of its length over a typical elastic length (see sidebar Rigid vs Flexible), and by the nature of the forcing, which depends on the ratio of the fiber length over the Kolmogorov length. The different regimes typically encountered are sketched in Figure 1, together with the range of applicability of currently-available experiments and simulations.

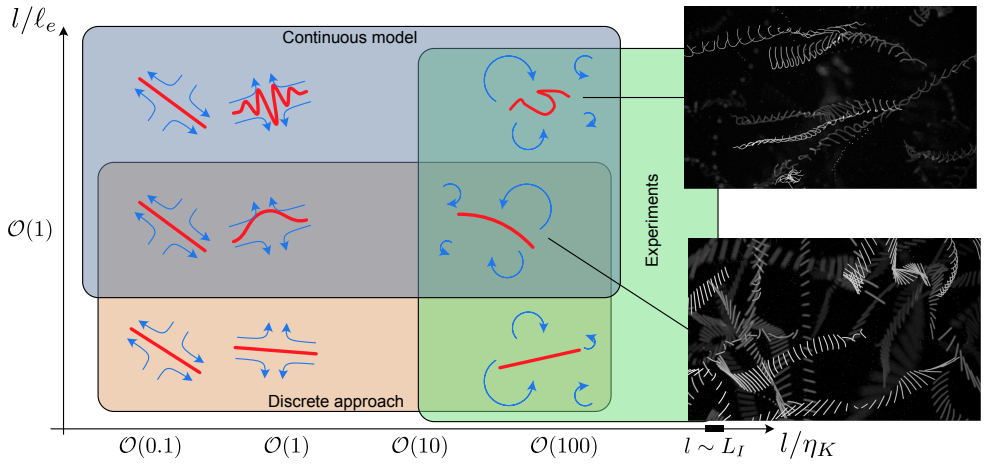


Figure 1

Sketch of the different regimes of deformation for a flexible fiber (red thick line), parameterized by the ratio of fiber length l to the linear elastic length ℓ_e, and optimal range of applicability of experiments and simulations, based on the ratio of fiber length l to Kolmogorov length scale η_K. The shaded areas highlight the complementarity among the different approaches within the parameter space. The upper boundary for l is represented by the integral length scale of the turbulent flow, L_I. Short fibers, for which $l/\eta_K \simeq \mathcal{O}(1)$ or smaller, typically experience a smooth flow. Deformations due to buckling instability are then triggered when the fiber is aligned with the compressive component of the rate of strain tensor (blue bent arrows). Long fibers, for which $l/\eta_K \gg \mathcal{O}(1)$ or smaller, experience a multiscale flow and simultaneously interact with many vortices (half-circle arrows): In this case, one or several bending modes can be excited depending on the fiber flexibility.

Rate of strain tensor: describes how a material deforms over time. Its eigenvectors represent the directions of maximum and minimum stretching or compression.The corresponding eigenvalues indicate the rate of deformation in those directions.

3. METHODOLOGIES

3.1. Experimental techniques

The fibers used in experiments at high Reynolds number flows are produced in a very similar way than those used in laminar flows. Most of the fibers are made of silicone or polydimethylsiloxane (PDMS), for which the linear elasticity approximation is valid over a wide range of deformations (Kim et al. 2011). The Young modulus can vary between few tens of kPa to hundreds of MPa. Currently, two main processes exist to produce fibers: molding and microfluidic processing. With molding, silicone or PDMS is injected into a cylindrical tube and remains until the end of the curing process. The inner diameter and length of the tube determine the final geometry of the fiber, allowing to produce fibers with diameters of about 150 μm or larger (Verhille & Bartoli 2016, Marchetti et al. 2018). This process is relatively easy to install but quite time-consuming and cannot be used to produce large amount of fibers. In contrast, the microfluidic technology allows to easily produce many elongated objects (Nunes et al. 2012, Mercader et al. 2010) albeit being more complicated and expensive to install. The diameter can be less than 100 μm with length of the order of few centimeters, a range that typically falls within the inertial scales of turbulence when compared to η_K, which varies between 50 and 500 μm in most experiments. To measure the 3D conformation of a flexible fiber, several synchronised high-speed cameras imaging the

same volume with different angles of view are generally used. To perform the 3D reconstruction, a model for the camera is needed to determine the position of a point in space from its projections onto the different images. The most classical one is the *pinhole model* (Faugeras & Luong 2001), also known as the Tsai model. In this model, the camera is characterized by eleven parameters: six extrinsic parameters for the position and orientation of the camera within the lab frame and five intrinsic parameters that correspond to the scaling factors converting the unit used in the lab (typically millimeters) to pixels, the coordinates of the pinhole projection onto the image plane and a skew coefficient (Verhille & Bartoli 2016). These different parameters needs to be determined by calibration. Note that this model can be refined to correct the optical distortion and the presence of different interfaces (Agrawal et al. 2012, Belden 2011). Other models have also been used to characterize the camera, but have not been employed for the reconstruction of flexible fibers (Machicoane et al. 2019, Pujara et al. 2021). From this model and the coordinate of the projection of the fiber onto the images, the 3D coordinates in space are determined either by matching each point along the fiber, as it is classically done in Particle Tracking (Verhille & Bartoli 2016), or by looking at the convex hull volume of the object, since it corresponds to the shape of the object for a fiber (Giurgiu et al. 2023, Masuk et al. 2021). The set of voxels is then fitted with a spline function or a polynomial function to determine the position of the centerline, as shown schematically in Figure 2.

3.2. Numerical approaches

The numerical approaches to simulate flexible fibers can be divided into discrete approach and continuum model, as shown schematically in Figure 3. Depending on the way forces and torques are computed, namely using models or directly, these approaches can be used to simulate point-wise fibers or fully-resolved fibers.

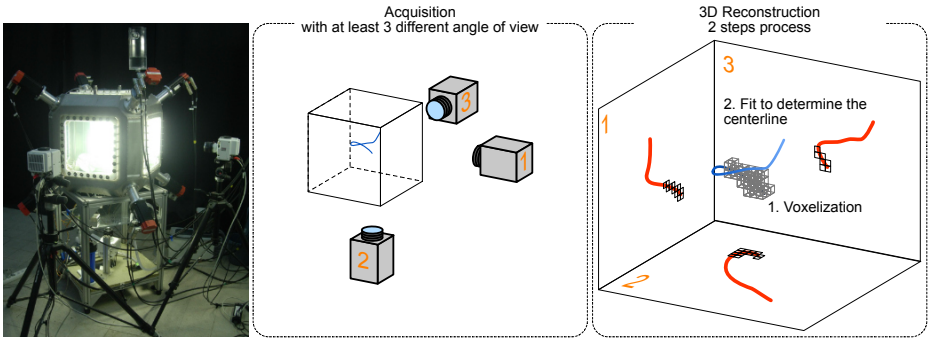


Figure 2

Experimental procedure for 3D reconstruction of a flexible fiber. The experimental setup (a typical setup for measurements in HIT is shown in the left-hand panel) must be equipped with at least three synchronized cameras with different angle of view for image acquisition (middle panel). The three images acquired are then used to obtain the shape of the deformed fiber as a set of voxels knowing the coordinate of the fiber projection on each image and the projection matrices of each camera (right-hand panel). The set of voxels is then fit using a spline or a polynomial function to determine the position of the centerline.

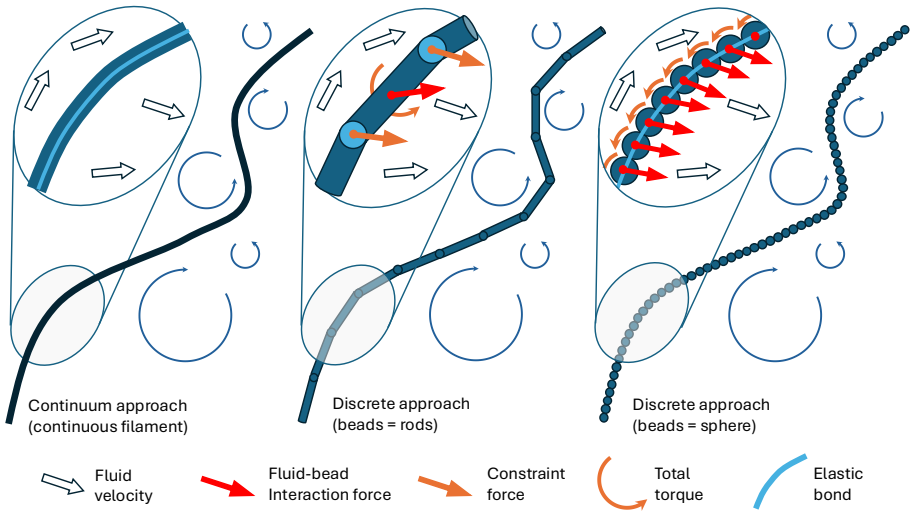


Figure 3

Sketch of the numerical approaches used to simulate flexible fibers interacting with turbulent vortices: The continuum approach represents fibers as continuous filaments that evolve subject to fluid-structure coupling forces and tensions; the discrete approach represents fibers as chains of elements (either rods or spheres) that evolve subject to forces, torques and elastic bonds.

3.2.1. Discrete approaches. The most common class of discrete approaches applies to cases in which Re_f is small but there is translational and rotational slip between the fiber and the fluid. These methods aim to describe a complex deformable object by the flexible assembly of simple rigid ones, generally composed of discrete elements (spheres or ellipsoids) interacting by some elastic and repulsive forces, but also with the surrounding fluid (Dotto & Marchioli 2019, Pei et al. 2018, Kunhappan et al. 2017, Andrić et al. 2014, 2013, Lindström & Uesaka 2009, 2007). The same type of approach has been used to discretize finite-size fibers (Tang et al. 2018, Delmotte et al. 2015, Favier et al. 2014, Wu & Aidun 2010, Huang et al. 2007) in combination with the Immersed Boundary Method - IBM (Peskin 1972), exploiting an external boundary force to impose the no-slip boundary condition at the fluid–solid interface, albeit not in turbulence with the exception of Sulaiman et al. (2017). With finite-size fibers, forces and torques are obtained directly from the fluid pressure and stresses distributions around the fibers, whereas suitable force and torque models are required for the application to point-wise fibers, as will be discussed below.

Considering an inertial frame of reference that uses a Cartesian coordinate system with axes $\{\mathbf{e}_x, \mathbf{e}_y, \mathbf{e}_z\}$, a generic element in the chain, labeled by subscript r hereinafter, is associated to a position vector $\mathbf{X}_r$ and is characterized by density ρ_f, cross-sectional diameter d, length $l_r = ||\mathbf{X}_r - \mathbf{X}_{r+1}||$ and aspect ratio $\Lambda_r = l_r/d$. For each element, the following dynamical equations of rigid-body motion for translation and rotation hold:

$$m_r \partial_t \mathbf{v}_r = \mathbf{F}_r^H + \mathbf{F}_r^B + \sum_s \mathbf{F}_{r,s}^I + \mathbf{F}_{r+1}^C - \mathbf{F}_r^C \,, \tag{7.}$$

$$\partial_t \left(\bar{\bar{\mathbf{J}}}_r \boldsymbol{\omega}_r \right) = \mathbf{T}_r^H + \sum_s \mathbf{T}_{r,s}^I + \mathbf{T}_{r+1}^b - \mathbf{T}_r^b + l_r \mathbf{X}_r \times \left(\mathbf{F}_{r+1}^C + \mathbf{F}_r^C \right) . \tag{8.}$$

In Equation 7, $m_r = \rho_f 2\pi\Lambda_r d^3$ is the mass of the element, $\mathbf{v}_r$ is the translation velocity evaluated at the center of mass of the element, denoted by vector $\mathbf{p}_r$, $\mathbf{F}_r^H$ is the hydrodynamic drag force exerted by the fluid surrounding the element, $\mathbf{F}_r^B$ is the body force (e.g. due to gravity), $\mathbf{F}_{r,s}^I$ is the interaction force due to contact or lubrication that is exerted on element r by element s of some other fiber or by a non-adjacent element of the same fiber, while $\mathbf{F}_{r+1}^C$ and $\mathbf{F}_r^C$ are the constraint forces produced by element $r+1$ on element r and by element r on element $r-1$, respectively. These forces ensure that the end points of adjacent elements overlap at all times and are obtained from the following connectivity constraint, which must be added to close the system of equations: $\mathbf{p}_r + l_r\mathbf{X}_r - (\mathbf{p}_{r+1} - l_{r+1}\mathbf{X}_{r+1}) = \mathbf{0}$.

In Equation 8, $\boldsymbol{\omega}_r$ is the angular velocity and $\bar{\bar{\mathbf{J}}}_r$ the inertia tensor of the element, which is typically computed as a function of its orientation. The first term on the right-hand side represents the hydrodynamic torque, $\mathbf{T}_r^H$, which can be split into a contribution due to the relative spin between the fiber and the surrounding fluid plus a contribution due to the action of the local fluid velocity gradients, respectively. The second term, $\mathbf{T}_{r,s}^I$, is the torque due to the interaction force $\mathbf{F}_{r,s}^I$. The two terms $\mathbf{T}_{r+1}^b$ and $\mathbf{T}_r^b$ represent the bending torque (a similar term can be added in case the twisting torque is not neglgible), while the last term, $l_r\mathbf{X}_r \times \left(\mathbf{F}_{r+1}^C + \mathbf{F}_r^C\right)$, is the torque contribution of the constraint forces.

The expressions used to compute forces and torques can be selected based on the element's Reynolds number, $Re_{f,r}$. Analytical solutions derived for an isolated axisymmetric ellipsoid can be used when $Re_{f,r} = 0$ (Kim & Karrila 2013) and extended to rod-like elements (Cox 1971). When $Re_{f,r} > 0$, inertial effects must be incorporated (Di Giusto et al. 2024), using for instance a suitably defined drag coefficient in the expression of $\mathbf{F}_r^D$ (Dotto & Marchioli 2019). For highly elongated fibers, other approaches are possible, namely the slender body theory (Batchelor 1970, Cox 1970), which can be used to obtain analytical approximations to the Stokes flow solution for fibers with large aspect ratio (Candelier et al. 2024, Andersson et al. 2021), or the resistive force theory (Kamal & Lauga 2023), which can be used to obtain the translation of any rigid slender body through a viscous fluid, provided that the radius of curvature is large compared with the body radius. The reader is referred to du Roure et al. (2019) for a complete description of these approaches.

Slender body theory: asymptotic technique that can be used to represent the disturbance velocity created by a particle as an integral of Stokeslets distributed along its axis.

3.2.2. Continuum model. An alternative approach is to model each fiber as a homogeneous, elastic filament that evolves according to a modified equation 1 in a Lagrangian framework, under the assumption of fiber inextensibility:

$$\partial_s\mathbf{X} \cdot \partial_s\mathbf{X} = 1\,. \qquad 9.$$

Equations 1 and 9 are an extended version of the distributed-Lagrange-multiplier/fictitious-domain formulation of the continuum equations introduced by Yu (2008). In this approach, the tension T is used to enforce fiber inextensibility and two terms need to be included in the force $\mathbf{F}$ on the right-hand-side of Equation 1: The fluid-structure coupling term (see sidebar Backreaction to the Flow) and the fluid acceleration $\rho\partial_t\dot{\mathbf{X}}$, used to cancel fluid inertia in the fictitious domain inside the fiber (Yu 2008). When dealing with multiple objects, filament-to-filament and filament-to-wall collisions must be accounted for as well. However, extensive testing of elastic and inelastic collision models have shown that, from a dynamical standpoint, filament-to-filament collisions are statistically irrelevant in dilute conditions and are therefore often neglected, while filament-to-wall collisions become marginally relevant only for highly flexible fibers (Olivieri et al. 2022b). Thus, it is often enough to account for them using a simple inelastic collision model, in which a repulsive force is applied to

the filament points approaching the wall within a range of four grid points: This model is usually called the *minimal collision model* (Snook et al. 2012). With the exception of the bending factor, which can be handled implicitly to permit larger time steps (Banaei et al. 2020b), the governing equations of motion can be solved using a two-step procedure (Huang et al. 2007): (i) solve a Poisson equation for the tension, obtained by combining Equations 1 and 9 (see Banaei et al. (2020b) for more details); (ii) solve Equation 1 to obtain the revised position of the Lagrangian points defining the filament. After discretising each fiber with N evenly-spaced, Lagrangian points (resulting in a spatial resolution that roughly corresponds to the Eulerian grid spacing), a 2nd-order finite-difference technique on a staggered grid for tension and position can be used to discretize the equations of motion (Huang et al. 2007, Banaei et al. 2020b, Olivieri et al. 2020). Recently, Agrawal et al. (2024) proposed a new framework to capture the large deformation dynamics of fibers. Using a geometrically exact, non-linear Euler-Bernoulli rod formulation, they showed that even a coarse mesh can

BACKREACTION TO THE FLOW

When the suspension of fibers is non-dilute, their backreaction to the flow must be accounted for. The mutual interactions between the fiber and the fluid is typically enforced via singular force distributions acting on each phase, often implemented in the setting of IBM for fully-resolved fibers (Huang et al. 2007, Pinelli et al. 2010, Banaei et al. 2020b, Olivieri et al. 2020, Agrawal et al. 2024). To do so, the equation of motion for the carrier flow, governed by the incompressible Navier-Stokes equations for a Newtonian fluid, are extended by including an additional force $\mathbf{f}_{\text{fs}}(\mathbf{x}, t)$ that mimics the presence of the solid phase. An equal and opposite force $\mathbf{F}$ must be present in the equation of motion for the fibers (Equation 1) to enforce the non-slip condition at their surface. This force can be computed as follows. The material points of the immersed fiber are forced to move with the fluid velocity at those points through a no-slip condition $\dot{\mathbf{X}} = \mathbf{u}(\mathbf{X}, t)$, with $\mathbf{X} = \mathbf{X}(s, t)$ the material point position and $\mathbf{u} = \mathbf{u}(\mathbf{x}, t)$ the fluid velocity. The fluid velocity at the position of the fiber Lagrangian point, $\mathbf{U} = \mathbf{u}(\mathbf{X}(s, t), t)$, is obtained by interpolating the fluid velocity at the Eulerian nodes surrounding the Lagrangian point as:

$$\mathbf{U}(\mathbf{X}(s,t),t) = \int \mathbf{u}(\mathbf{x},t)\delta(\mathbf{x} - \mathbf{X}(s,t))\mathrm{d}^3\mathbf{x}, \tag{10.}$$

where the δ is the Dirac delta function. Using $\mathbf{U}$, the fluid-structure forcing term can be obtained as $\mathbf{F}(s, t) = \kappa(\mathbf{U} - \dot{\mathbf{X}})$, where κ is a large negative constant (Goldstein et al. 1993, Olivieri et al. 2020). Finally, the forcing on the fluid from the fiber is calculated as:

$$\mathbf{f}_{\text{fib}}(\mathbf{x},t) = \frac{1}{\rho}\int_s \mathbf{F}(s,t)\delta(\mathbf{x} - \mathbf{X}(s,t))\mathrm{d}s. \tag{11.}$$

The coupling between the fluid and the fiber surface is attained spreading the force distribution computed by means of a Lagrangian IBM over the Eulerian grid points, enforcing the no-slip condition at the Lagrangian points representing the filaments. The interface between the fluid and the fiber is therefore not sharply captured, but diffused among the grid points by means of a window function. Based on this, one can estimate an effective filament diameter of about three grid points, namely $d = 3\Delta x$ in units of the Eulerian grid spacing. An improved coupling algorithm to properly enforce the fiber diameter was presented by Pinelli et al. (2010), a method which also allows for a larger order of accuracy.

deliver accurate results, leading to a major gain in computational efficiency.

4. FIBER DEFORMATION

Elongated fibers transported by a turbulent flow may experience fluid velocity changes along their length. This is particularly true for fibers with length within the inertial subrange of turbulence, referred to as *long fibers* hereinafter, for which the velocity variation is non-linear and the forcing is multiscale. These fibers are expected to behave differently from those with length of the order of the Kolmogorov length or smaller, referred to as *short fibers* hereinafter, which are in the viscous subrange of turbulence. Flexibility represents an additional source of bias in determining the macroscopic outcome of fiber-turbulence interaction, e.g. in terms of overall fiber deformation, motion and spatial distribution within the flow. In this section, we review fiber deformation by highlighting the different deformation regimes and their statistical characterization.

Inertial subrange:: region of the turbulent kinetic energy spectrum in which turbulent kinetic energy is purely transferred to smaller scales, where it is eventually dissipated.

Viscous (or dissipation) subrange: region of the turbulent kinetic energy spectrum in which molecular viscosity becomes important and viscous dissipation of kinetic energy takes place.

4.1. Deformations of short fibers

The deformation statistics generally depend on fiber flexibility but also on the ratio between the particle length and the Kolmogorov length. However, as small elongated objects tend to align preferentially with the extensional direction of the rate-of-strain tensor (Voth & Soldati 2017), short fibers remain straight for most of the time because they experience smooth velocity gradients as they are brought about by the flow. Still, buckling instabilities can be triggered when the fiber is aligned with the compressive direction of the rate-of-strain tensor. Allende et al. (2018) have shown that the selected mode of buckling and the probability of its occurrence $\mathcal{P}_{\rm buck}$ are governed by the ratio:

$$\mathcal{F} = \frac{8\pi\mu l^4}{cB\tau_K}\,, \qquad 12.$$

where $c = -(1 - 2\log\Lambda) \gg 1$. The probability distribution of buckling events follows an exponential law of the type: $\mathcal{P}_{\rm buck} \propto \exp[A(\mathcal{F}/\mathcal{F}^\star)^{1/2}]$, which is linked to the probability distribution of the velocity gradients in turbulence.

4.2. Deformations of long fibers

The system is richer for long fibers as they experience non-uniform forcing. In this case, two deformation regimes have been identified (Gay et al. 2018, Rosti et al. 2018a,b, Olivieri et al. 2022b): The first regime corresponds to moderately flexible fibers and only the first bending mode is excited, the second to large deformations associated to fully 3D conformation. These regimes are discussed next with reference to Figure 4.

4.2.1. Weakly flexible fibers: planar conformation. In the under-damped regime, the deformation timescale, defined as the main frequency of the Fourier transform of the end-to-end distance (Rosti et al. 2018a), corresponds to the frequency of the first mode of vibration. In contrast, there is no temporal signature of this bending mode in the over-damped regime as viscous dissipation prevents oscillations. The main frequency in the over-damped regime corresponds to the typical timescale of the turbulent eddies of size l: $\omega_l = l/u_l \sim (l/\eta_K)^{2/3}\tau_K^{-1}$, see Figure 4c (Olivieri et al. 2021, 2022b). In both regimes, the average conformation is a U shape similar to the first bending mode with maximum

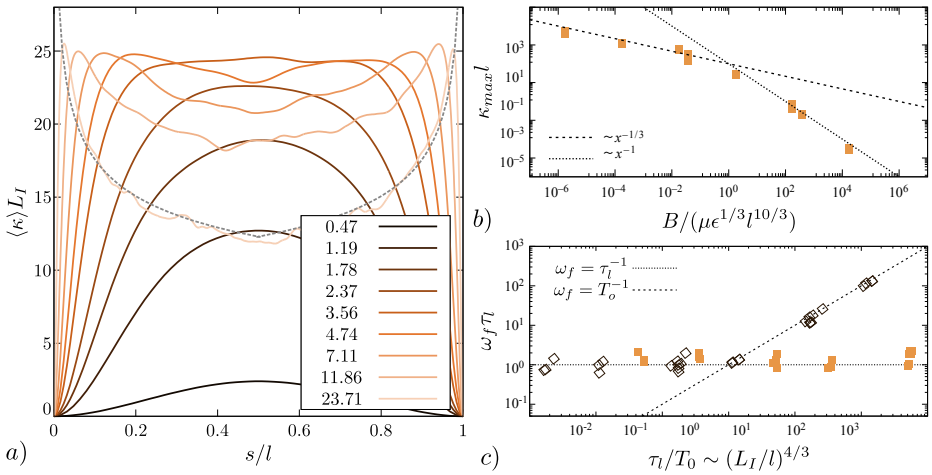


Figure 4

Panel *a*): Evolution of the mean curvature, as function of the normalized curvilinear coordinate, s/l, at varying fiber length. The fiber length increases from darker to lighter orange. The dashed line corresponds to the $s^{-2/9}$ scaling, see Equation 16. Panel *b*): Evolution of the mean maximal curvature in the over-damped regime ($St \ll 1$) as a function of the ratio $(L_v/l)^{10/3}$. Panel *c*): Evolution of the timescale of deformation as a function of the ratio between the forcing timescale, τ_l, and the period of oscillation, T_o. The filled symbols correspond to fiber in the over-damped regime ($St \ll 1$), the empty symbols to the under-damped regime ($St \gg 1$). From: Gay et al. (2018), Olivieri et al. (2022a).

curvature at the center of the fiber, $s = l/2$, and zero curvature at the extremities, $s = 0$ and $s = l$, due to the boundary condition, see Figure 4a (Gay et al. 2018). Brouzet et al. (2014) have proposed an analogy between the deformation of flexible fibers in turbulence and that of semi-flexible polymers distorted by thermal fluctuation (Doi & Edwards 1986). Indeed, as for semi-flexible polymers (or worm-like polymer chains), the end-to-end distance is governed by the ratio of the fiber length l over a typical length that is called persistence length, ℓ_p, in polymer theory (Yamakawa 1971) and is equivalent to the linear elastic length ℓ_e introduced in Section 2. However, if ℓ_p can be interpreted as a balance between the thermal energy and the elastic energy stored inside the polymer, this is not the case for ℓ_e, for which the balance of energy must be replaced by a balance of power. Indeed, in a stationary flow regime, the energy $\mathcal{E}$ of the system composed of the fibers is on average constant and its rate of change over time must obey the condition:

$$\partial_t \mathcal{E} = \mathcal{P}_{\text{inj}} - \mathcal{P}_{\text{dis}} = 0\,, \tag{13.}$$

where $\mathcal{P}_{\text{inj}}$ and $\mathcal{P}_{\text{dis}}$ are the power received (resp. given) by the system from (to) turbulence. The power injected by turbulence is proportional to the ratio of the energy contained in an eddy of size l over the lifetime of the structure: $\tau_l = l/u_l$. The dissipated power is proportional to the ratio of the elastic energy stored inside the fiber, which can be expressed as $\int B\kappa^2(s)\mathrm{d}s$ over the lifetime of the deformation, given by the bending relaxation time in the over-damped regime and the first bending mode frequency in the under-damped regime (Verhille 2022). Defining the linear elastic length ℓ_e as the length for

which $\int \kappa^2(s)\mathrm{d}s = 1/\ell_e$, the following relation can be obtained in the over-damped regime:

$$\rho \ell_e^3 \epsilon = \frac{EI}{\ell_e \tau_b(\ell_e)} \;\Rightarrow\; \ell_e = \frac{B^{1/4}}{(\rho\mu\epsilon)^{1/8}}\,, \tag{14.}$$

where $\tau_b(\ell_e)$ is the bending relaxation time of a fiber with length ℓ_e, see Equation 3. It is interesting to note that, even if ℓ_e has a different physical interpretation for long and short fibers, it has the same expression (*cf.* Equation 12 for $\mathcal{F} = 1$ and Equation 14). The power balance also allows to predict the evolution of the mean curvature, κ, as function of the fiber length for intermediate flexibility (Brouzet et al. 2021):

$$\kappa \sim \frac{(\rho\mu\epsilon)^{1/2} l^3}{B} = \frac{l^3}{\ell_e^4}\,. \tag{15.}$$

4.2.2. Highly flexible fibers: 3D conformations. The mean deformation of very flexible fibers, *i.e.* fibers with length $l \gg \ell_e$, are enslaved to the turbulent fluctuations. Rosti et al. (2018a) showed that tracking the fiber extremities in the under-damped regime allows to measure the longitudinal structure function. This opens new possibility to use fiber as a proxy for turbulence. It is also a natural extension of the work by Brizzolara et al. (2021), who proposed to use the tumbling of rigid fibers to measure the transverse structure function. The possibility of measuring the structure function in the over-damped regime has not been considered yet. However, it has been shown that in such regime the enslavement of deformation to the turbulent fluctuations leads to a straightening of the fiber. Indeed, the mean curvature along the fiber length, $\kappa(s)$, increases from the extremities towards the center, where a maximum is reached, for flexible fibers ($l \sim \ell_e$) as shown in Figure 4a (darker curves). For very flexible fibers ($l \gg \ell_e$ corresponding to the curves with lighter color in Figure 4), the curvature increases from the extremities, reaches a maximum at approximately one linear elastic length ($s \simeq \ell_e$ and $s \simeq l - \ell_e$) and decreases to a minimum at the center (Gay et al. 2018). Once again, a power balance can be used to understand this apparent stiffening. Due to fiber inextensibility, a local deformation caused by a small eddy will be accompanied by a global rearrangement of the fiber conformation. This rearrangement is at the origin of an additional viscous dissipation that scales as $\mu\epsilon^{1/3}s^{4/3}B\kappa^3(s)$, increasing with the fiber length l. For long fibers, the viscous dissipation can therefore be larger than bending, and will then determine the amplitude of the mean curvature according to the following scaling relation:

$$\kappa(s) \sim \left(\frac{\rho}{B}\right)^{1/6} \epsilon^{1/9} s^{-2/9}\,. \tag{16.}$$

In the Euler-Bernoulli equation, this non local contribution appears in the tension term T. As detailed in section 2, this term has two contributions: The tangential force, $\int f_\parallel(s)\mathrm{d}s$, responsible for the stiffening, and a resistive term to bending, $B\kappa^2$, which acts as a non-linear spring (Marheineke & Wegener 2007). In the over-damped regime, the transition from moderately flexible to highly flexible fibers occurs when both the linear and non-linear terms have the same amplitude: $\kappa \sim L_v^{-1}$, where L_v is a characteristic length scale referred to as non-linear viscous elastic length, defined as:

$$L_v = \frac{B^{3/10}}{\mu^{3/10}\epsilon^{1/10}}\,. \tag{17.}$$

Tumbling and spinning: The rotation modes of an axisymmetric particle are naturally decomposed into two components perpendicular to the symmetry axis, called tumbling, and one component along the symmetry axis, called spinning or drilling.

This definition has been validated by numerical simulations (Gay et al. 2018). In summary, for $l \sim \ell_e$ the mean curvature increases when the length is increased as $\kappa \sim l^3/\ell_e^4$, while for $l \gg L_v$ the mean curvature decreases when the fiber length is increased as $\kappa \sim l^{-2/9}/\eta_K^{2/9} L_v^{5/9}$. It might seem counter-intuitive that in the non-linear regime the mean curvature is smaller than in the linear regime. However, Olivieri et al. (2022a) studied the evolution of the mean of the maximum curvature $\kappa_{\max}$ experienced by a fiber and found that the maximum curvature scales as $\kappa_{\max}^l \sim (\mu\epsilon^{1/3} l^{10/3}/B)^\alpha$ with $\alpha = 1$ in the linear regime and $\alpha = 1/3$ in the non-linear regime. Then, even if the exponent for very flexible fiber is lower than the one for the linear regime, it is still positive and therefore the mean maximum curvature continuously increases, as shown in Figure 4b. The different vales of the exponent can be found by balancing the viscous forcing and the linear or non-linear elastic term in Equation 1. A similar evolution for the mean of the maximum curvature has been observed in the under-damped regime (Olivieri et al. 2022b). However, inertia and the presence of bending wave makes the problem more complex to analyze (Audoly & Neukirch 2005). Moreover, in the under-damped regime, the transition lengthscale between the two regimes of deformations has been shown to be equal to (Rosti et al. 2018a):

$$L_i = \frac{B^{3/8}}{\epsilon^{1/4}(\rho_f d^2)^{3/8}} \,. \tag{18.}$$

This non-linear inertial length has been interpreted as the one for which the forcing timescale and the period of oscillation are equal. Note that this temporal argument in the over-damped regime can be also used to define the transition length-scale and leads to the same non-linear viscous length L_v defined previously. Finally, it is important to remark that fiber deformation, as well as its overall dynamics, is also modulated by the density difference between the fiber and fluid, which has a twofold effect. First, the density mismatch affects the dynamical regime that characterizes the fiber (over-damped or under-damped, see Section 2). Second, it controls the period of oscillation T_o (see Equation 6) which determines the two subregimes present in the under-damped regime, see Figure 4.

5. FIBER MOTION

Fiber dispersion in turbulent flow has been investigated mostly for the case of rigid fibers modeled as rods or ellipsoids, focusing on phenomena such as preferential alignment and preferential concentration (Voth & Soldati 2017, Marchioli et al. 2016). The understanding of these phenomena is rather complete for sub-Kolmogorov fibers. However, much less is known for long fibers, especially for lengths comparable to the flow scales within the inertial range, a limit that is relevant for the case of flexible fibers and has been addressed only recently (Chiarini et al. 2024). In this section, we survey the phenomenology of the motion of flexible fibers in turbulence, addressing specifically the features that characterize their collective dispersion behavior. In fact, settling of flexible heavy fibers in turbulence has received scarce attention Banaei et al. (2020a): This is clearly an area ripe for future development.

5.1. Fiber spatial distribution

The spatial distribution attained by fibers in a turbulent flow is generally non-uniform and modulated by several concurrent factors, in particular fiber inertia. Inertial fibers tend to

CLUSTERING AND CAUSTICS

In particle-laden flows, one of the cluster formation mechanisms is clustering by caustics. Caustics are phase-space singularities that, akin to caustics in geometrical optics, result in anomalous particle number density fields and large relative velocities at small separations, causing the spatial continuum descriptions of the inertial particle velocity field to fail (Falkovich et al. 2002, Wilkinson & Mehlig 2005).

concentrate preferentially and form clusters within the flow. In confined flows, their distribution is non-uniform also along the wall-normal direction, possibly leading to segregation in the wall region. These mechanisms, which have been widely investigated for spherical particles (Soldati & Marchioli 2009), are examined next to highlight the distinctiveness of flexible fibers.

5.1.1. Preferential concentration and clustering. Up to now, the analysis of preferential concentration and clustering has been carried out in the limit of dilute suspensions, in which fiber-fiber interactions due to collisions are negligible. In the case of HIT, the spatial distribution of long fibers is associated to the preferential sampling of vortical flow structures provided that fibers are longer than the dissipation scale but not much longer than the vortex tubes (Picardo et al. 2018, 2020). Bending stiffness has no effect because the fibers do not need to coil in order to thread a vortex tube and align with its axis. This is not true in 2D turbulence, where bending stiffness is found to prevent coiling and reduce preferential sampling (Picardo et al. 2018). Note that clustering in 2D flows is dependent on both the Stokes number and the fiber aspect ratio, and is strongly correlated with the formation of velocity caustics, namely singularities in which fibers are focused in thin filaments that resemble the optical caustics formed by deflection of sunlight by water waves (Martínez et al. 2017), see the sidebar Clustering and Caustics. In the case of extensible fibers that can be stretched out by the flow, these also preferentially sample the intense, tubular, vortex filaments of 3D turbulence, in particular for lengths up to inertial-range scales. Such fibers extend in vortical regions and follow axially stretched tubular vortices by aligning with their axes (Picardo et al. 2020, Singh et al. 2020).

Olivieri et al. (2022b) observed a systematic increase of clustering at increasing fiber flexibility (i.e. decreasing the bending stiffness) and, as expected, for inertial fibers. This clustering is always associated to a preferential alignment between the local orientation of the fibers and the strain rate principal directions: Both the alignment with the first or second principal direction (namely the direction of maximum extension or intermediate extension/compression, respectively) and the anti-alignment with the third principal direction (maximum compression direction) typically increase when the fibers become more rigid, this increase being observed also when moving from heavy to neutrally buoyant fibers. Similar conclusions were obtained for the case of wall-bounded flow by Dotto & Marchioli (2019) and Dotto et al. (2020), who observed that flexible fibers exhibit a stronger tendency than rigid fibers to accumulate in the very-near-wall region, where they appear to be trapped by the same inertia-driven mechanisms that govern the preferential concentration of spherical particles and rigid fibers in bounded flows. In such region, the bending of flexible fibers increases as inertia decreases, and fiber deformation appears to be controlled by mean shear

and turbulent Reynolds stresses. Preferential segregation into low-speed streaks and preferential orientation in the mean flow direction is also observed, as discussed in Sec. 5.1.2.

5.1.2. Wall accumulation and segregation. In wall-bounded turbulence, fibers tumble and collide with solid boundaries, bouncing off with an impulse that propels them toward the center of the flow, similar to pole vaulting. For short fibers, the resulting spatial distribution is determined by a balance between this bounce-off drift and the turbophoretic drift (Bec et al. 2024, Marchioli & Soldati 2002) that controls wall accumulation for inertial particles, especially those with sub-Kolmogorov size. As shown by Dotto & Marchioli (2019) and Dotto et al. (2020), flexible fibers with length significantly smaller than the inertial subrange of turbulence still undergo a net wallward drift but the peak of near-wall concentration is much weaker compared to spherical particles (Marchioli & Soldati 2002, Bec et al. 2024) and rigid fibers (Marchioli et al. 2010, Dhas & Marchioli 2025). Sub-Kolmogorov spherical particles can penetrate much deeper inside the viscous sublayer and this facilitates their long-term trapping into low-speed fluid streaks (Dotto & Marchioli 2019, Di Giusto & Marchioli 2022). Super-Kolmogorov spherical particles cannot do that and their wall-accumulation is limited by an excluded-volume geometric effect, which prevents the formation of strong accumulation regions due to the dis-alignment between fiber orientation and the straining regions of the flow. In principle, rigid fibers could execute efficient pole vaulting but their capability to escape is limited by the tendency to enter the near-wall layer with a shallow angle and to align parallel to the wall. Remarkably, wall accumulation is not observed for long fibers, which are more efficient than short fibers in exploiting the bounce-off drift allowed by pole vaulting and thus exhibit a stronger tendency to migrate away from the walls. This dynamics produces depleted regions near the boundaries and more concentrated regions in the bulk. As shown by Bec et al. (2024), these higher concentrations in the channel center result in a greater net flux of fibers than what was initially imposed by the fluid, this effect being more pronounced as fiber length increases. It should be noted that long fibers can sample different regions of the flow simultaneously, namely portions of the fiber located at different wall distances experience different average fluid velocities. For inextensible fibers, this implies that portions located closer to the channel center, where the mean velocity is higher, tend to pull the whole fiber. On the other hand, portions closer to the walls, where the mean velocity is lower, tend to slow it down. This results in a higher fiber streamwise velocity than the fluid near the walls and lower in the center, as observed in Figure 5.

5.2. Fiber preferential alignment

Preferential alignment has been investigated in terms of alignment with the stretching and compressing directions within the flow (mostly in HIT) but also in terms of alignment with the flow directions (in wall-bounded turbulence). Results obtained in HIT by Olivieri et al. (2022b) indicate that the vorticity is mostly aligned with the intermediate eigenvector and orthogonal to the direction of maximum compression, i.e. the third eigenvector, while only a minimal departure is observed for the alignment with the first eigenvector, corresponding to the direction of maximum extension. The main difference that can be observed between neutrally buoyant fibers and heavier-than-fluid fibers is the mild attenuation of the alignment of vorticity with the intermediate eigenvector in the latter case, as well as a weakening of the preferential alignment of fibers with the strain rate. Similar behavior is observed in

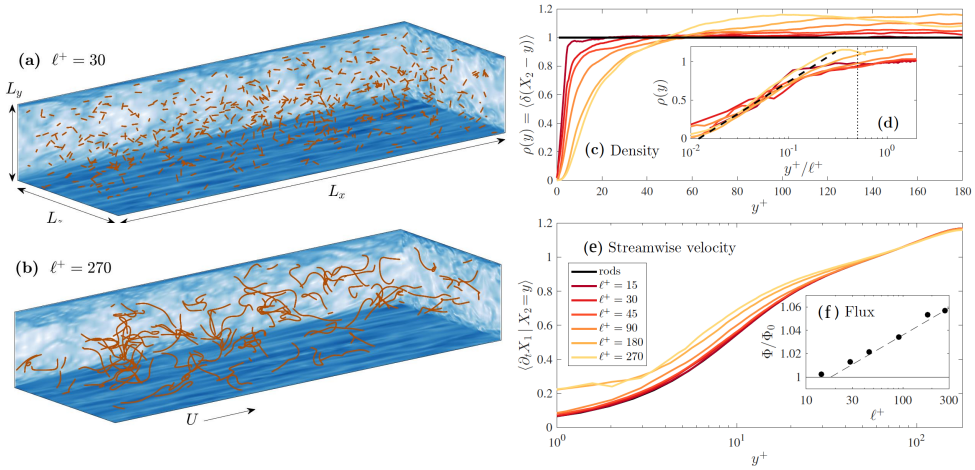


Figure 5

Panels (a)-(b): Instantaneous distribution of flexible fibers with length $l^+ = 30$ and $l^+ = 270$ in wall units. The colormap shows the modulus of fluid vorticity in the bounding planes. Panel (c): Average fiber number density as a function of the distance to the wall, y^+, at varying fiber length, also shown as a function of y^+/l^+ in the inset (d), where the dashed line shows the $\log l^+$ scaling. Panel (e): Average fiber velocity in the streamwise direction as a function of y^+. The inset (f) shows the normalized fiber fluxes, obtained combining the concentration and velocity profiles: The logarithmic scaling (dashed line) shows an increase of the flux by few percents for fibers whose lengths are within the log-layer of the wall. From: Bec et al. (2024).

viscoelastic turbulence, in which flexible fibers interact with stretching polymers (Aswathy & Rosti 2024): the neutrally buoyant fibers show a higher alignment with the polymer stretching directions compared to the denser ones. In wall-bounded turbulence, fibers tend to preferentially align with the streamwise flow direction and perpendicular to the mean shear, this trend being more evident for longer fibers. Away from the walls, a weaker preferential alignment is observed because the flow becomes more homogeneous and isotropic (Dotto & Marchioli 2019, Dotto et al. 2020).

5.3. Fiber rotation

Similarly to rigid fibers (Oehmke et al. 2021, Shin & Koch 2005), the rotation of a flexible fiber is related closely to its orientational dynamics and tendency to align preferentially with the flow. Up to now, the rotation of flexible fibers has been investigated for wall-bounded turbulence, where the flow anisotropy plays a major role in determining fiber tumbling and spinning. Dhas & Marchioli (2025) have recently shown that fibers with negligible inertia tend to experience higher tumbling and spinning rates close to the wall than near the channel center. Further, longer fibers exhibit higher rotation rates, whereas the introduction of rigidity tends to have the opposite effect. This is associated to slower changes in orientation experienced by the flexible fibers, in view of their tendency to migrate

away from the wall, compared to their rigid counterparts, which tend to stay closer to the wall and are thus subject to stronger mean shear. However, the rotation of the longer fibers is found to be less sensitive to their flexibility/rigidity as they move and orient themselves similarly, irrespective of their bending stiffness. The rotation rates of the fibers exhibit a clear dependence on flexibility and length in the bulk of the flow. The effect of length vanishes in the case of rigid fibers. Owing to the strong turbulence fluctuations that occur close to the wall and to fiber-wall collisions, fibers in that region tend to tumble and spin at rates significantly higher than those closer to the channel center.

6. THE ROLE OF FLEXIBILITY ON FIBER-TURBULENCE INTERACTIONS

The collective dynamics of flexible fibers in fluid flows can lead to macroscopic effects that are of relevance in a number of situations of practical interest. Notable examples are, for instance, fractionation (Lundell et al. 2011) and entanglement/flocculation (Switzer & Klingenberg 2004, Cui & Grace 2007). Of the many macroscopic phenomena that could be addressed, here we focus on two problems that have attracted the attention of researchers and for which progress has been made in connecting microscopic fiber dynamics to the macroscopic phenomena of interest: fragmentation and turbulence modulation.

6.1. Fragmentation

The discussion made so far has focused on fibers that exhibit a Hookean behavior and undergo linear elastic deformations that satisfy the condition $\kappa d \ll 1$. In this section, we want to address the fragmentation of brittle fibers that break when undergoing large deformations. For a brittle fiber, breakup occurs as soon as the applied stress causing deformation reaches a maximum value, called the yield stress σ_b. This kind of particle is a good model to investigate the fragmentation of microplastics in the sea, which have been weathered by UV, salt, ozone and micro-organisms. In numerical simulations, this parameter can be adjusted to explore a range of regimes from tough to very fragile materials. In the experiments, the yield stress is a distributed value, and its mean can be varied by changing the material of the fiber and/or the density of defects (Brouzet et al. 2021). So far, only the fragmentation of fibers in the over-damped regime has been investigated. As discussed in Section 2, the modes of deformation and the statistics differ for short and long fibers, leading to distinct breakup scenarios.

As short fibers preferentially align with the elongational component of the rate-of-strain tensor, they are mainly stretched by the flow. In this case, the stress is equal to zero at the fiber extremities and increases quadratically to reach a maximum value at the fiber center. When the stress exceeds the yield stress, the fiber breaks into two fragments of equal length (Allende et al. 2020). Another breaking mode is observed when short fibers align with the compressive direction of the rate-of-strain tensor triggered by the buckling instability. For this type of deformation, the stress σ is proportional to the local curvature κ, i.e., $\sigma \sim \kappa d$. In this configuration, the fiber can break into several fragments, with the number of fragments depending on the excited buckling mode, the local intensity of the velocity gradient, and the stiffness of the fiber (Allende et al. 2020).

For long fibers, three scenarios have been identified based on the fiber brittleness. The first one corresponds to fibers with high yield strain, which requires curvatures higher than the maximum curvature a flexible fiber can sustain before being broken. The second scenario

involves very fragile fibers that can break at curvatures much smaller than $1/\ell_e$, thus forming fragments much smaller than the elastic length. In this case, the typical fragment size is expected to be given by the mean curvature of the fiber, which scales as $\kappa_{\max} \sim l^3/\ell_e^4$. The third scenario corresponds to an intermediate regime in which the maximum curvature before breaking is $\kappa_{\max} \sim 1/\ell_e$. In this context, Brouzet et al. (2021) modeled the evolution of the fragment size distribution over time using a Smoluchowski equation:

$$\partial_t n_\ell = -p(\ell) n_\ell + \int 2p(\ell_>)\gamma(\ell, \ell_>)\, \mathrm{d}\ell_> \,, \tag{19.}$$

where n_ℓ is the number of fragments of size ℓ, $p(\ell)$ is the probability that a fiber of length ℓ breaks, and $\gamma(\ell, \ell_>)$ is the probability that a fiber of length $\ell_>$ breaks into two parts, one of length ℓ and one of length $\ell_> - \ell$. The probability $p(\ell)$ can be estimated using the curvature distribution, while $\gamma(\ell, \ell_>)$ can be derived from the evolution of the mean curvature along the fiber length (Brouzet et al. 2021). Ultimately, the final distribution corresponds to a relatively peaked distribution with a maximum length of the order of ℓ_e. The research on the fragmentation of long fibers has, so far, been focused on the fragment size distribution and the evaluation of the fragmentation rate is still an open question.

6.2. Turbulence modulation

Most research on the dynamics of particles dispersed in turbulence has focused on dilute suspensions, in which the flow is unaffected by the presence of the dispersed phase. In this situation, a *one-way* coupling approach can be adopted, which greatly simplifies the modeling of the problem. However, for relatively high concentrations, one must take into account the *two-way* coupled problem: In addition to the particles being transported and distorted by the flow, the flow is also changed by their back-reaction, because of the no-slip condition at the particle surface (Balachandar & Eaton 2010, Maxey 2017, Brandt & Coletti 2022). Focusing on the specific case of anisotropic particles and fibers, relatively few studies have examined the modulation of turbulence under non-dilute conditions (Andersson et al. 2012, Ardekani et al. 2017, Olivieri et al. 2020, 2021, 2022b), showing a significant deviation from the conventional phenomenology seen for a strictly Newtonian fluid. More specifically, Olivieri et al. (2021, 2022b) have methodically explained how the back-reaction of the dispersed phase impacts the macroscopic behavior of the carrier flow, demonstrating a general depletion of turbulent kinetic energy that is mirrored by the (decreasing) micro-scale Reynolds number of the flow. The mass fraction of the suspension, given by the ratio of the mass of the suspended fibers to the total mass of the suspension (which is thus a combination of the density ratio and volume fraction), rather than other factors like the number density, controls the back-reaction, noting indeed that at number densities corresponding to the so-called "diluted regime" (Butler & Snook 2018), the back-reaction effect can already be non-negligible. The energy spectra, reported in Figure 6, show two robust features when the mass fraction increases: A relative increase in the small-scale energy content and an overall large-scale energy depletion. The energy fluxes in Fourier space (see sidebar Multiscale Energy Balance) provide a good explanation for this evidence: As the mass fraction increases, the non-linear term is suppressed and the energy transfer directly related to the fluid-solid coupling becomes more significant. Surprisingly, the flexibility of the fibers seems to have a rather small, but consistent, impact, with a weaker back-reaction for more flexible fibers. From the physical viewpoint, a more relaxed flow-structure coupling (i.e., fibers are more responsive to the action of the flow) results from greater flexibility (i.e.,

reducing γ), which is reflected in a less noticeable back-reaction when compared to the rigid case. In general, flexibility may be claimed to be of secondary importance in the modulation of the carrier flow because the variation with γ seems to be quite modest.

Olivieri et al. (2022a) and Cannon et al. (2024) discovered that the drop in the turbulent kinetic energy and micro-scale Reynolds number with increasing mass fraction is comparable to that produced by spherical particles of the same length. The authors demonstrated that the sphere diameter or fiber length is the representative lengthscale at which the fluid-solid coupling is prominent for both types of dispersed objects. However, while the back-reaction for finite-size spherical objects is usually limited to relatively large scales, with a small change of the higher-wavenumber inertial and viscous subrange, the complete energy spectrum is altered with finite-size fibers, as a result of their ability to transport energy down to the lowest scales of the flow. This difference can be simply understood by considering that the immersed objects subtract energy from the flow by means of hydrodynamic drag and then re-inject it through their wakes. Spheres produce a turbulent wake that contributes to the classical energy cascade, since this occurs entirely within the inertial subrange. The transfer for fibers occurs instead at much smaller scales, where viscosity takes over, thus inhibiting the contribution of the non-linear term. Cannon et al. (2024) examined the vorticity and shear of the local flow structures to determine their shape. In addition to producing strong vortical and shearing structures that counteract the typical vortex stretching behavior, the authors discovered that the fibers increase local shear and dissipation in structures that have dimensions larger than one but less than two, a possible source of the increased flow intermittency. Cannon et al. (2024) also examined how the Reynolds number affected the modulation of turbulence: Fibers modulate turbulence even in the weakest turbulent flows ($Re \to 0$), with the majority of observables converging to the single-phase result as $Re \to \infty$, except for the modulation of turbulent kinetic energy, in which the Reynolds number has little to no effect. Note that the multiscale effect carried by the fibers in a turbulent flow has been found also in the case of canopy flows, when the fibers are clamped to the wall (Monti et al. 2023, Foggi Rota et al. 2024a,b, Foggi Rota et al. 2025).

When considering channel flows, only a few studies have examined the potential reduction of turbulent friction losses by the addition of fibers (Paschkewitz et al. 2004, 2005,

MULTISCALE ENERGY BALANCE

The scale-by-scale energy transfer for a two-phase flow can be written as:

$$\mathcal{P}(k) + \Pi(k) + \Pi_{\mathrm{fs}}(k) + \mathcal{D}(k) = \epsilon\,, \tag{20.}$$

where the various terms appearing on the left hand side are the production rate $\mathcal{P}$ (here associated with the external forcing used to sustain the flow and typically acting only at the largest scales, i.e., low wavenumbers), the energy flux Π associated with the non-linear term, the energy flux Π_{fs} associated with the fluid-solid coupling, and the viscous dissipation $\mathcal{D}$. In the single-phase case $\Pi_{\mathrm{fs}} \equiv 0$, and the dominant terms in the balance are the non-linear term Π and the viscous dissipation D when approaching the lowest and highest wavenumbers, respectively. See Pope (2001) for a full derivation of the single-phase equation and Olivieri et al. (2020) for the extension to the case with fibers.

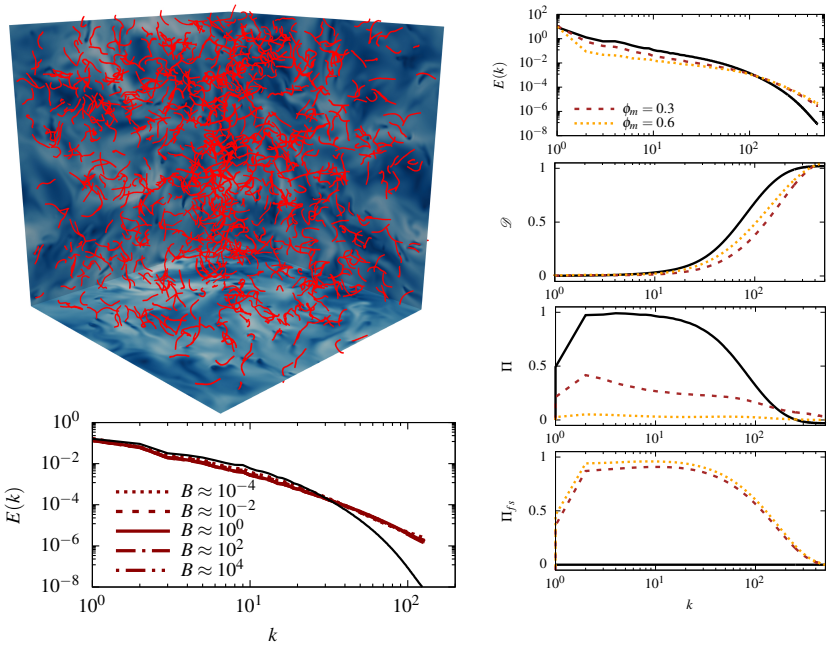


Figure 6

Top-left panel: Snapshot from DNS of finite-size flexible fibers (in red) dispersed in HIT. The length of the fiber is comparable to the inertial range of scales. Bottom-left panel: The energy spectra for a suspension of fibers with different bending modulus, B. Right-end panels (top to bottom): Energy spectra, fluid dissipation, non-linear energy flux, and fluid-solid interaction contribution for different values of the mass fraction, ϕ_m. In these panels, the black curves correspond to the unladen case. From: Olivieri et al. (2022b).

Di Giusto & Marchioli 2022, Gillissen et al. 2008, Moosaie & Manhart 2013, Di Giusto & Marchioli 2022), inspired by the vast amount of work done with polymers; see, e.g., White & Mungal (2008) and Benzi & Ching (2018), with fibers providing little drag reduction or requiring significantly higher concentrations to achieve the same drag reduction. Paschkewitz et al. (2004) were among the first to investigate the drag reduction caused by rigid neutrally buoyant fibers, modeling their influence with lengths significantly shorter than all scales of turbulent flow. They found that the fibers weaken and enlarge the near-wall vortex structures, and reduce drag by producing a force contrary to the Newtonian acceleration. The effectiveness of short stiff rods in reducing drag was experimentally proven by (Paschkewitz et al. 2005), reporting a 10% reduction in drag. In light of these encouraging findings, Moosaie & Manhart (2013) created a two-way coupling modeling method for a diluted suspension of rigid fibers and further validated the previous findings. In a more recent study, Di Giusto & Marchioli (2022) discovered that employing substantially longer fibers can similarly reduce drag in a turbulent channel flow, with smaller volume fractions.

7. CONCLUSIONS AND PERSPECTIVES

Flexible fibers in turbulence present a rich source of problems in terms of local and non-local interactions with the fluid. These interactions result in a number of complex phenomena that can be investigated only using sophisticated experimental and numerical techniques. Also complicated are the theories through which fiber dynamics can be understood and modeled. To close our review, we summarize the main takeaways and future issues.

SUMMARY POINTS

1. Flexible fibers in high Reynolds number flows are found in many environmental and industrial problems of practical interest, and are receiving a growing attention from the multiphase flow community. To study these problems, it is possible to leverage on the experimental and numerical tools that have been developed for the investigation of elongated non-spherical particles (rigid fibers, in particular), extending their applicability to include flexibility effects.
2. Flexibility can be characterized by two main length scales: The linear elastic length, ℓ_e, and the non-linear viscous elastic length, ℓ_v. These scales can be used to discriminate between the different fiber deformation regimes that characterize fiber motion. In particular, ℓ_v represents a threshold between smooth (C-shaped or U-shaped) deformations and more complex deformations.
3. Flexibility has an effect on macroscopic phenomena such as wall-accumulation and preferential concentration, which exhibit both qualitative and quantitative differences with respect to the case of spherical particles and rigid fibers. This happens because the sampling of the turbulent flow by the fibers is governed by non-local dynamics associated to their length and stiffness, differently from rigid fibers that are governed by local dissipative dynamics.
4. Long fibers experience a varying flow field along their length. When fibers are rigid, their inability to deform acts like a coarse-graining high-pass filter that makes fibers insensitive to the small scales of the flow. Flexibility removes this filter and allows fibers to respond to the small scales. This implies that the local features of the flow play a role in determining the dynamics of individual fibers.
5. While flexibility is a key feature to understand the fiber dynamics, the effect of the fibers on the turbulent flow seems to be less affected by the fiber deformation, where mass and volume fraction are the most determinant factors.

FUTURE ISSUES

1. An important aspect that requires attention has to do with the lack of uniformity of the averaging procedures adopted to compute the statistics and even the definition of important quantities such as the fiber response time and Reynolds number. Different averaging procedures and definitions are found in the literature, making comparison of results difficult or even misleading. This review offers a first step towards a unifying framework, but additional efforts are certainly needed.
2. Generally speaking, the macroscopic consequences of fiber dynamics in turbulence are still poorly understood. This is especially true for flexible fibers, for which

only a minor proportion of the parameter space has been explored so far. As a consequence, there is a knowledge gap that prevents connecting applications to the fundamental governing mechanisms.

3. Models capable of handling realistic calculations of the full shape of the fiber and its aerodynamic coefficients are required to boost the reliability of numerical simulations. Also needed are models that can deal with shape asymmetries (e.g. curved fibers with fore-aft asymmetry) and account for their effect on the inertial torques and angular dynamics of the fibers.
4. A particular need in experiments is the ability to relate the dynamics of individual particles to macroscopic effects such as turbulence modulation (possibly including the effect of fiber extensibility) or rheological effects in dense suspensions.
5. For problems involving inertial flexible fibers in turbulence, little is known about how their dynamics are altered in finite Froude number conditions (i.e., when the gravitational forces are not negligible).
6. Future effort should be also devoted to the analysis of deformable objects with shapes different from the elongated cylindrical fibers addressed in this review, for which stretching and twisting can play an important role (e.g. flexible disks in turbulence). To tackle this problem, experimental techniques are being developed already but no suitable generalization of the discrete or continuous approaches discussed in this review has been developed yet.

DISCLOSURE STATEMENT

The authors are not aware of any affiliations, memberships, funding, or financial holdings that might be perceived as affecting the objectivity of this review.

ACKNOWLEDGMENTS

C.M. thankfully acknowledges financial support from the European Union-NextGeneration EU PRIN 2022, "Next-generation multiscale modelling of dense emulsions for enhanced multiphase flow processes" 20229WJBPS - E53D23002940006.
M.E.R. is supported by the Okinawa Institute of Science and Technology Graduate University (OIST) with subsidy funding from the Cabinet Office, Government of Japan.

LITERATURE CITED

Agrawal A, Ramalingam S, Taguchi Y, Chari V. 2012. A theory of multi-layer flat refractive geometry. *IEEE Conference on Computer Vision and Pattern Recognition* :3346–3353

Agrawal V, Kulachenko A, Scapin N, Tammisola O, Brandt L. 2024. An efficient isogeometric/finite-difference immersed boundary method for the fluid–structure interactions of slender flexible structures. *Comput. Methods Appl. Mech. Eng.* 418:116495

Allende S, Henry C, Bec J. 2018. Stretching and buckling of small elastic fibers in turbulence. *Phys. Rev. Lett.* 121:154501

Allende S, Henry C, Bec J. 2020. Dynamics and fragmentation of small inextensible fibres in turbulence. *Philos. Trans. A Math. Phys. Eng. Sci.* 378(2175):20190398

Andersson H, Celledoni E, Ohm L, Owren B, Tapley B. 2021. An integral model based on slender body theory, with applications to curved rigid fibers. *Phys. Fluids* 33:041904

Andersson H, Zhao L, Barri M. 2012. Torque-coupling and particle–turbulence interactions. *J. Fluid Mech.* 696:319–329

Andrić J, Fredriksson S, Lindström S, Sasic S, Nilsson H. 2013. A study of a flexible fiber model and its behavior in dns of turbulent channel flow. *Acta Mech.* 224:2359

Andrić J, Lindström S, Sasic S, Nilsson H. 2014. Rheological properties of dilute suspensions of rigid and flexible fibers. *J. Non-Newt. Fluid Mech.* 212:36

Ardekani M, Costa P, Breugem W, Picano F, Brandt L. 2017. Drag reduction in turbulent channel flow laden with finite-size oblate spheroids. *J. Fluid Mech.* 816:43–70

Aswathy M, Rosti ME. 2024. The dynamics of fibres dispersed in viscoelastic turbulent flows. *J. Fluid Mech.* 984:A72

Audoly B, Neukirch S. 2005. Fragmentation of rods by cascading cracks: Why spaghetti does not break in half. *Phys. Rev. Lett.* 959:095505

Audoly B, Pomeau Y. 2010. Elasticity and geometry. Oxford University Press

Balachandar S, Eaton J. 2010. Turbulent dispersed multiphase flow. *Annu. Rev. Fluid Mech.* 42(1):111–133

Banaei A, Rahmani M, Martínez D, Brandt L. 2020a. Inertial settling of flexible fiber suspensions. *Phys. Rev. Fluids* 5(2):024301

Banaei A, Rosti ME, Brandt L. 2020b. Numerical study of filament suspensions at finite inertia. *J. Fluid Mech.* 882:A5

Batchelor G. 1970. Slender-body theory for particles of arbitrary cross-section in stokes flow. *J. Fluid Mech.* 44(3):419–440

Bec J, Brouzet C, Henry C. 2024. Enhanced transport of flexible fibers by pole vaulting in turbulent wall-bounded flow. *Phys. Rev. Fluids* 9:L062501

Belden J. 2011. Calibration of multi-camera systems with refractive interfaces. *Exp. Fluids* 54:1463

Benzi R, Ching E. 2018. Polymers in fluid flows. *Annu. Rev. Condens. Matter Phys.* 9:163–181

Bergfreund J, Wobill C, Lebreton L, Windhab E, Evers F, et al. 2024. Impact of microplastic pollution on breaking waves. *Phys. Fluids* 36:072108

Bhowmick T, Seesing J, Gustavsson K, Guettler J, Wang Y, et al. 2024. Inertia induces strong orientation fluctuations of non-spherical atmospheric particles. *Phys. Rev. Lett.* 132:034101

Brandt L, Coletti F. 2022. Particle-laden turbulence: Progress and perspectives. *Annu. Rev. Fluid Mech.* 54:159–189

Brizzolara S, Rosti ME, Olivieri S, Brandt L, Holzner M, Mazzino A. 2021. Fiber tracking velocimetry for two-point statistics of turbulence. *Phys. Rev. X* 11(3):031060

Brouzet C, Guiné R, Dalbe MJ, Favier B, Vandenberghe N, et al. 2021. A laboratory model for plastic fragmentation in the turbulent ocean. *Phys. Rev. Fluids* 6:024601

Brouzet C, Verhille G, Le Gal P. 2014. Flexible fiber in a turbulent flow: A macroscopic polymer. *Phys. Rev. Lett.* 112:074501

Butler J, Snook B. 2018. Microstructural dynamics and rheology of suspensions of rigid fibers. *Annu. Rev. Fluid Mech.* 50:299–318

Candelier F, Gustavsson K, Sharma P, Sundberg L, Pumir A, et al. 2024. Torques on curved atmospheric fibres. *Phys. Rev. Res.* 7:013179

Cannon I, Olivieri S, Rosti ME. 2024. Spheres and fibers in turbulent flows at various Reynolds numbers. *Phys. Rev. Fluids* 9(6):064301

Chen Z, Liu Y, Sung H. 2024. Enhancement of heat transfer by a buckled flexible filament in a channel flow. *Int. J. Heat Mass Transfer* 224:125364

Chiarini A, Rosti ME, Mazzino A. 2024. Dynamics and applications of finite-size fibre-like objects in turbulent flows. *Eur. J. Mech. B Fluids* 108:104–118

Cox R. 1970. The motion of long slender bodies in a viscous fluid. Part 1. General theory. *J. Fluid Mech.* 44:791

Cox R. 1971. The motion of long slender bodies in a viscous fluid. Part 2. Shear flow. *J. Fluid Mech.* 45:625

Cui H, Grace J. 2007. Flow of pulp fibre suspension and slurries: A review. *Int. J. Multiphase Flow* 33:921–934

Delmotte B, Climent E, Plouraboué F. 2015. A general formulation of bead models applied to flexible fibers and active filaments at low Reynolds number. *J. Comput. Phys.* 286:14–37

Dhas D, Marchioli C. 2025. Orientational dynamics of long flexible fibers in wall-bounded turbulence. *J. Fluids Eng.* 147(7):071102

Di Giusto D, Bergougnoux L, Marchioli C, Guazzelli E. 2024. Influence of small inertia on Jeffery orbits. *J. Fluid Mech.* 979:A42

Di Giusto D, Marchioli C. 2022. Turbulence modulation by slender fibers. *Fluids* 7(8):255

Doi M, Edwards S. 1986. The theory of polymer dynamics. Oxford Univ. Press

Dotto D, Marchioli C. 2019. Orientation, distribution, and deformation of inertial flexible fibers in turbulent channel flow. *Acta Mech.* 230:597–621

Dotto D, Soldati A, Marchioli C. 2020. Deformation of flexible fibers in turbulent channel flow. *Meccanica* 55:343–356

du Roure O, Lindner A, Nazockdast E, Shelley M. 2019. Dynamics of flexible fibers in viscous flows and fluids. *Annu. Rev. Fluid Mech.* 51:539

Falkovich G, Fouxon A, Stepanov MG. 2002. Acceleration of rain initiation by cloud turbulence. *Nature* 419:151–154

Faugeras O, Luong QT. 2001. The geometry of multiple images. The MIT Press

Favier J, Revell A, Pinelli A. 2014. A lattice boltzmann–immersed boundary method to simulate the fluid interaction with moving and slender flexible objects. *J. Comput. Phys.* 261:145–161

Foggi Rota G, Chiarini A, Rosti ME. 2025. Reconfiguration and dynamics of clamped fibers under finite-amplitude surface gravity waves. *Physical Review Fluids* 10(1):014301

Foggi Rota G, Koseki M, Agrawal R, Rosti ME. 2024a. Forced and natural dynamics of a clamped flexible fiber in wall turbulence. *Phys. Rev. Fluids* 9:L012601

Foggi Rota G, Monti A, Olivieri S, Rosti ME. 2024b. Dynamics and fluid–structure interaction in turbulent flows within and above flexible canopies. *J. Fluid Mech.* 989:A11

Gay A, Favier B, Verhille G. 2018. Characterisation of flexible fibre deformations in turbulence. *Europhys. Lett.* 123:24001

Gillissen J, Boersma B, Mortensen P, Anderson H. 2008. Fibre-induced drag reduction. *J. Fluid Mech.* 602:209–218

Giurgiu V, Caridi G, Alipour M, De Paoli M, Soldati A. 2023. The TU Wien turbulent water channel: Flow control loop and three-dimensional reconstruction of anisotropic particle dynamics. *Rev. Sci. Instrum.* 94:095101

Giurgiu V, Caridi G, De Paoli M, Soldati A. 2024. Full rotational dynamics of plastic microfibers in turbulence. *Phys. Rev. Lett.* 132:054101

Goldstein D, Handler R, Sirovich L. 1993. Modeling a no-slip flow boundary with an external force field. *J. Comp. Phys.* 105(2):354–366

Huang W, Shin S, Sung H. 2007. Simulation of flexible filaments in a uniform flow by the immersed boundary method. *J. Comp. Phys.* 226(2):2206–2228

Kamal C, Lauga E. 2023. Resistive-force theory of slender bodies in viscosity gradients turbulence. *J. Fluid Mech.* 963:A24

Kim S, Karrila S. 2013. Microhydrodynamics: Principles and selected applications. Butterworth-Heinemann, Stoneham

Kim T, Kim J, Jeong O. 2011. Measurement of nonlinear mechanical properties of pdms elastomer. *Microelectron. Eng.* 88:1982–1985

Kunhappan D, Harthong B, Chareyre B, Balarac G, Dumont P. 2017. Numerical modelling of high aspect ratio flexible fibers in inertial flows. *Phys. Fluids* 29:093302

Landau L, Lifshitz E. 1959. Theory of elasticity. Pergamon Press

Lindström S, Uesaka T. 2007. Simulation of the motion of flexible fibers in viscous fluid flow. *Phys. Fluids* 19:113307

Lindström S, Uesaka T. 2009. A numerical investigation of the rheology of sheared fiber suspensions. *Phys. Fluids* 21:083301

Lundell F, Söderberg L, Alfredsson P. 2011. Fluid mechanics of papermaking. *Annu. Rev. Fluid Mech.* 43:195–217

Machicoane N, Aliseda A, Volk R, Bourgoin M. 2019. A simplified and versatile calibration method for multi-camera optical systems in 3D particle imaging. *Rev. Sci. Instrum.* 90(3):035112

Marchetti B, Raspa V, Lindner A, du Roure O, Bergougnoux L, et al. 2018. The deformation of a flexible fiber settling in a quiescent viscous fluid. *Phys. Rev. Fluids* 3:104102

Marchioli C, Fantoni M, Soldati A. 2010. Orientation, distribution and deposition of elongated, inertial fibers in turbulent channel flow. *Phys. Fluids* 22(3):232

Marchioli C, Soldati A. 2002. Mechanisms for particle transfer and segregation in a turbulent boundary layer. *J. Fluid Mech.* 468:283 – 315

Marchioli C, Zhao L, Andersson H. 2016. On the relative rotational motion between rigid fibers and fluid in turbulent channel flow. *Phys. Fluids* 28(1):013301

Marheineke N, Wegener R. 2007. Modeling and application of a stochastic drag for fibers in turbulent flows. *Int. J. Multiphase Flow* 37(2):136–148

Martínez M, Vernet A, Pallares J. 2017. Clustering of long flexible fibers in two-dimensional flow fields for different stokes numbers. *Int. J. Heat Mass Transf.* 111:532

Masuk A, Salibindla A, Ni R. 2021. Simultaneous measurements of deforming hinze-scale bubbles with surrounding turbulence. *J. Fluid Mech.* 910:A21

Maxey M. 2017. Simulation methods for particulate flows and concentrated suspensions. *Annu. Rev. Fluid Mech.* 49:171–193

Mercader C, Lucas A, Derré A, Zakri C, Moisan S, et al. 2010. Kinetics of fiber solidification. *Proc. Nat. Acad. Sci.* 107(43):18331–18335

Monti A, Olivieri S, Rosti ME. 2023. Collective dynamics of dense hairy surfaces in turbulent flow. *Sci. Rep.* 13(1):5184

Moosaie A, Manhart M. 2013. Direct Monte Carlo simulation of turbulent drag reduction by rigid fibers in a channel flow. *Acta Mech.* 224:2385–2413

Nunes J, Sadlej K, Tama J, Stone H. 2012. Control of the length of microfibers. *Lab Chip* 12(13):2301–2304

Oehmke T, Bordoloi A, Variano E, Verhille G. 2021. Spinning and tumbling of long fibers in isotropic turbulence. *Phys. Rev. Fluids* 6:044610

Olivieri S, Brandt L, Rosti ME, Mazzino A. 2020. Dispersed fibers change the classical energy budget of turbulence via nonlocal transfer. *Phys. Rev. Lett.* 125(11):114501

Olivieri S, Cannon I, Rosti ME. 2022a. The effect of particle anisotropy on the modulation of turbulent flows. *J. Fluid Mech.* 950:R2

Olivieri S, Mazzino A, Rosti ME. 2021. Universal flapping states of elastic fibers in modulated turbulence. *Phys. Fluids* 33:071704

Olivieri S, Mazzino A, Rosti ME. 2022b. On the fully coupled dynamics of flexible fibres dispersed in modulated turbulence. *J. Fluid Mech.* 946:A34

Parrella F, Brizzolara S, Holzner M, Mitrano D. 2024. Impact of heteroaggregation between microplastics and algae on particle vertical transport. *Nat. Water* 2:541–552

Paschkewitz J, Dimitropoulos C, Hou Y, Somandepalli V, Mungal M, et al. 2005. An experimental and numerical investigation of drag reduction in a turbulent boundary layer using a rigid rodlike polymer. *Phys. Fluids* 17:085101

Paschkewitz J, Dubief Y, Dimitropoulos C, Shaqfeh E, Moin P. 2004. Numerical simulation of turbulent drag reduction using rigid fibres. *J. Fluid Mech.* 518:281–317

Pei Z, Zhang Y, Zhou J. 2018. A model for the particle-level simulation of multiple flexible fibers moving in a wall-bounded fluid flow. *J. Fluids Struct.* 80:37–58

Peskin C. 1972. Flow patterns around heart valves: a numerical method. *J. Comput. Phys.* 10(2):252–271

Picardo J, Singh R, Ray Samriddhi S, Vincenzi D. 2020. Dynamics of a long chain in turbulent flows: Impact of vortices. *Philos. Trans. A Math. Phys. Eng. Sci.* 378:20190405

Picardo J, Vincenzi D, Pal N, Ray Samriddhi S. 2018. Preferential sampling of elastic chains in turbulent flow. *Phys. Rev. Lett.* 121:244501

Pinelli A, Naqavi I, Piomelli U, Favier J. 2010. Immersed-boundary methods for general finite-difference and finite-volume Navier-Stokes solvers. *J. Comput. Phys.* 229(24):9073–9091

Pope SB. 2001. Turbulent flows. Cambridge University Press

Powers T. 2010. Dynamics of filaments and membranes in a viscous fluid. *Rev. Mod. Phys.* 82(2):1607–1631

Pujara N, Du Clos K, Ayres S, Variano E, Karp-Boss L. 2021. Measurements of trajectories and spatial distributions of diatoms (Coscinodiscus spp.) at dissipation scales of turbulence. *Exp. Fluids* 62:149

Rosti ME, Banaei A, Brandt L, Mazzino A. 2018a. Flexible fiber reveals the two-point statistical properties of turbulence. *Phys. Rev. Lett.* 121:044501

Rosti ME, Olivieri S, Banaei A, Brandt L, Mazzino A. 2018b. Flowing fibers as a proxy of turbulence statistics. *Meccanica* 55:357–370

Shin M, Koch D. 2005. Rotational and translational dispersion of fibres in isotropic turbulent flows. *J. Fluid Mech.* 540:143–173

Singh R, Gupta M, Picardo J, Vincenzi D, Ray S. 2020. Sedimenting elastic filaments in turbulent flows. *Phys. Rev. E* 101:053105

Snook B, Guazzelli E, Butler J. 2012. Vorticity alignment of rigid fibers in an oscillatory shear flow: Role of confinement. *Phys. Fluids* 24(12):121702

Soldati A, Marchioli C. 2009. Physics and modelling of turbulent particle deposition and entrainment: Review of a systematic study. *Int. J. Multiphase Flow* 35(9):827–839

Sugathapala M, Capuano T, Brandt L, Iudicone D, Sardina G. 2025. Vertical transport of buoyant microplastic particles in the ocean: The role of turbulence and biofouling. *Environ. Pollut.* 369:125819

Sulaiman M, Climent E, Delmotte B, Fede P, Plouraboué F, Verhille G. 2017. Numerical modelling of long flexible fibers in homogeneous isotropic turbulence. *Eur. Phys. J. E* 42:132

Switzer L, Klingenberg D. 2004. Flocculation in simulations of sheared fiber suspensions. *Int. J. Multiphase Flow* 30:67–87

Tang Y, Wu TH, He GW, Qi D. 2018. Multi-flexible fiber flows: A direct-forcing immersed boundary lattice-boltzmann lattice-spring approach. *Int. J. Multiphase Flow* 99:408–422

Tatsii D, Bucci S, Bhowmick T, Guettler J, Bakels L, et al. 2023. Shape matters: Long-range transport of microplastic fibers in the atmosphere. *Environ. Sci. Technol.* 58:671 – 682

Verhille G. 2022. Deformability of discs in turbulence. *J. Fluid Mech.* 933:A3

Verhille G, Bartoli A. 2016. 3D conformation of a flexible fiber in a turbulent flow. *Exp. Fluids* 57:117

Voth G, Soldati A. 2017. Anisotropic particles in turbulence. *Annu. Rev. Fluid Mech.* 49:249

White C, Mungal M. 2008. Mechanics and prediction of turbulent drag reduction with polymer additives. *Annu. Rev. Fluid Mech.* 40:235–256

Wilkinson M, Mehlig B. 2005. Caustics in turbulent aerosols. *Europhys. Lett.* 71:186–192

Wu J, Aidun C. 2010. A method for direct simulation of flexible fiber suspensions using lattice boltzmann equation with external boundary force. *Int. J. Multiphase Flow* 158:104262

Xu D, Wang B, Yu Z, Guo Y. 2008. Clustering in gas-fluidized riser flows of flexible fibers. *AIChE J.* 69(4):e18024

Yamakawa H. 1971. Modern theory of polymer solutions. Harper & Rows

Yu Z. 2008. A DLM/FD method for fluid/flexible-body interactions. *J. Comput. Phys.* 207(1):1–27